nature communications

Article

https://doi.org/10.1038/s41467-024-55149-2

Mammalian SLC39A13 promotes ER/Golgi iron transport and iron homeostasis in multiple compartments

Received: 17 May 2023

Accepted: 2 December 2024

Huihui Li[1], Yanmei Cui[1], Yule Hu[1], Mengran Zhao[2], Kuanyu Li[3], Xiaoyun Pang[4], Fei Sun[4] & Bing Zhou[1,5]

Iron is a potent biochemical, and accurate homeostatic control is orchestrated by a network of interacting players at multiple levels. Although our understanding of organismal iron homeostasis has advanced, intracellular iron homeostasis is poorly understood, including coordination between organelles and iron export into the ER/Golgi. Here, we show that SLC39A13 (ZIP13), previously identified as a zinc transporter, promotes intracellular iron transport and reduces intracellular iron levels. ZIP13 loss causes an iron deficiency in the ER/Golgi and other intracellular compartments, such as lysosomes and mitochondria, as well as elevating iron in the cytosol. ZIP13 overexpression has the opposite effect, increasing iron in organellar compartments. We suggest that ZIP13 gatekeeps an iron trafficking route that shunts iron from the cytosol to the ER/Golgi hub. *Zip13*-knockout male mice have iron deposition in several tissues. These data demonstrate that mammalian ZIP13 is crucial for iron homeostasis and suggest a potential iron transport function.

Iron (Fe) is an essential trace element for almost all living organisms due to its role in many important physiological activities, including DNA synthase, oxygen transport, respiration and ATP production[1–3]. Iron homeostasis is tightly regulated, requiring the participation of many iron metabolism-related proteins. Within a cell, iron homeostasis, in particular intracellular iron partitioning, is generally not well understood. In mammals, mitochondrial iron uptake is mediated by mitoferrin, plus a proposed lysosome-mitochondria contact or the kiss-and-run mechanism[4]. Cytosolic iron is exported to the exterior by ferroportin (FPN1), the only so far reported iron exporter in mammalian cells. As a result, FPN1 has been shown to remove cytosolic iron and play essential roles in systemic iron homeostasis by releasing iron from the cells of the duodenum, spleen, and liver to the blood[5–8].

SLC39A, or ZIP (zinc/iron permease), is a family of proteins primarily involved in zinc transport, but some of them, such as ZIP8 and ZIP14, have been reported to transport other metal ions, including iron, cadmium, and manganese ions[9–13]. A few years ago, we reported that the fruit fly (*Drosophila melanogaster*) ZIP13 (dZIP13) is responsible for supplying iron to load the fly ferritin[14–18], which is exported through the classical secretory pathway to deliver iron for the systemic use. The fly appears to have a divergent iron homeostasis system in that it has secreted ferritin, no apparent transferrin receptor, no apparent hepcidin, and no FPN1 homolog[19–21]. It is considered that mammalian FPN1 and the fly ZIP13-ferritin axis function as two alternatives for iron export and are likely the only ones in their respective systems. Indeed, mutation in *Fpn1* almost disables iron export in the mouse intestine, crippling iron absorption from the diet[6], whereas in the fly, the *Zip13* mutation leads to severe iron deficiency, rescuable by excessive iron supplement[17]. In mammals, ferritin is not in the classical secretory compartments, and it is known that cytosolic PCBPs in the cytosol help ferritin iron loading instead[22]. Despite that ZIP13's ability in transporting zinc has been investigated and established[15,17,23–26], we

---

[1]Shenzhen Institute of Synthetic Biology, Shenzhen Institutes of Advanced Technology, Chinese Academy of Sciences, Shenzhen 518055, China. [2]Beijing Key Laboratory for Precancerous Lesion of Digestive Disease, Department of Gastroenterology, Beijing Friendship Hospital, Capital Medical University, Beijing, China. [3]Jiangsu Key Laboratory of Molecular Medicine, Medical School of Nanjing University, Nanjing 210093, China. [4]National Key Laboratory of Biomacromolecules, CAS Center for Excellence in Biomacromolecules, Institute of Biophysics, Chinese Academy of Sciences, Beijing 100101, China. [5]Faculty of Synthetic Biology, Shenzhen University of Advanced Technology, Shenzhen 518055, China. e-mail: bing.zhou@siat.ac.cn

wondered whether mammalian ZIP13 is additionally involved in any way in iron homeostasis. We surprisingly found that mammalian ZIP13 not only promotes iron transport to the ER/Golgi but also acts as a central player in gating an unrecognized iron passage route that regulates iron homeostasis in multiple intracellular compartments. ZIP13 appears to fulfill unique and much broader iron physiology functions in vivo than anticipated.

Results

ZIP13 over-expression reduces cytosolic iron levels

To analyze mammalian ZIP13's role in iron homeostasis, we overexpressed human ZIP13 (hZIP13) in mouse embryonic fibroblasts (MEFs). The cytosolic labile iron pool (LIP) significantly decreased after hZIP13 overexpression (Fig. 1a, b, and Supplementary Fig. 1a). This also occurred when dZIP13 was overexpressed (Fig. 1a). Consistently, biochemical evidence revealed that the protein levels of iron-regulated protein (IRP) 1 and transferrin receptor 1 (TfR1) slightly increased, and the levels of FPN1, H-ferritin (FtH), and L-ferritin (FtL) decreased, indicating a cytosolic iron deficiency in these cells (Fig. 1c, d). However, the expression of IRP2 did not change (Fig. 1c). Iron deficiency also affects aconitase (a Fe-S protein) activities, which could be used as a molecular indicator for intracellular iron availability[17]. As shown in Fig. 1e, the activity of mitochondrial aconitase did not appreciably change, but the cytosolic aconitase activity significantly dropped after ZIP13 overexpression, consistent with a lack of cytosolic iron. The co-expression of P58 (Golgi marker) indicated that the overexpressed hZIP13 mainly overlapped with the Golgi apparatus in the MEFs (Fig. 1f). After ZIP13 transfection, the Golgi iron increased (Fig. 1b, g, and Supplementary Fig. 1a). These results were also confirmed in HeLa cells (Supplementary Fig. 1b). In contrast, enforced expression of human ZIP7 (hZIP7) or *Drosophila* ZIP7 (dZIP7), an evolutionarily closely related ER/Golgi-resident zinc transporter[27,28], only affected the zinc but not iron levels (Supplementary Fig. 1c–e). Moreover, overexpression of hZIP13 did not affect the mRNA levels of other ZIP family members tested, including possible iron transporters, such as *Zip7*, *Zip8*, and *Zip14* control, which transports zinc ions (Supplementary Fig. 1f). These results suggest mammalian ZIP13 can promote iron transport from the cytosol to the secretory pathway under physiological iron concentrations, and is prominently involved in iron homeostasis. It is somewhat surprising that the intracellular iron level was so

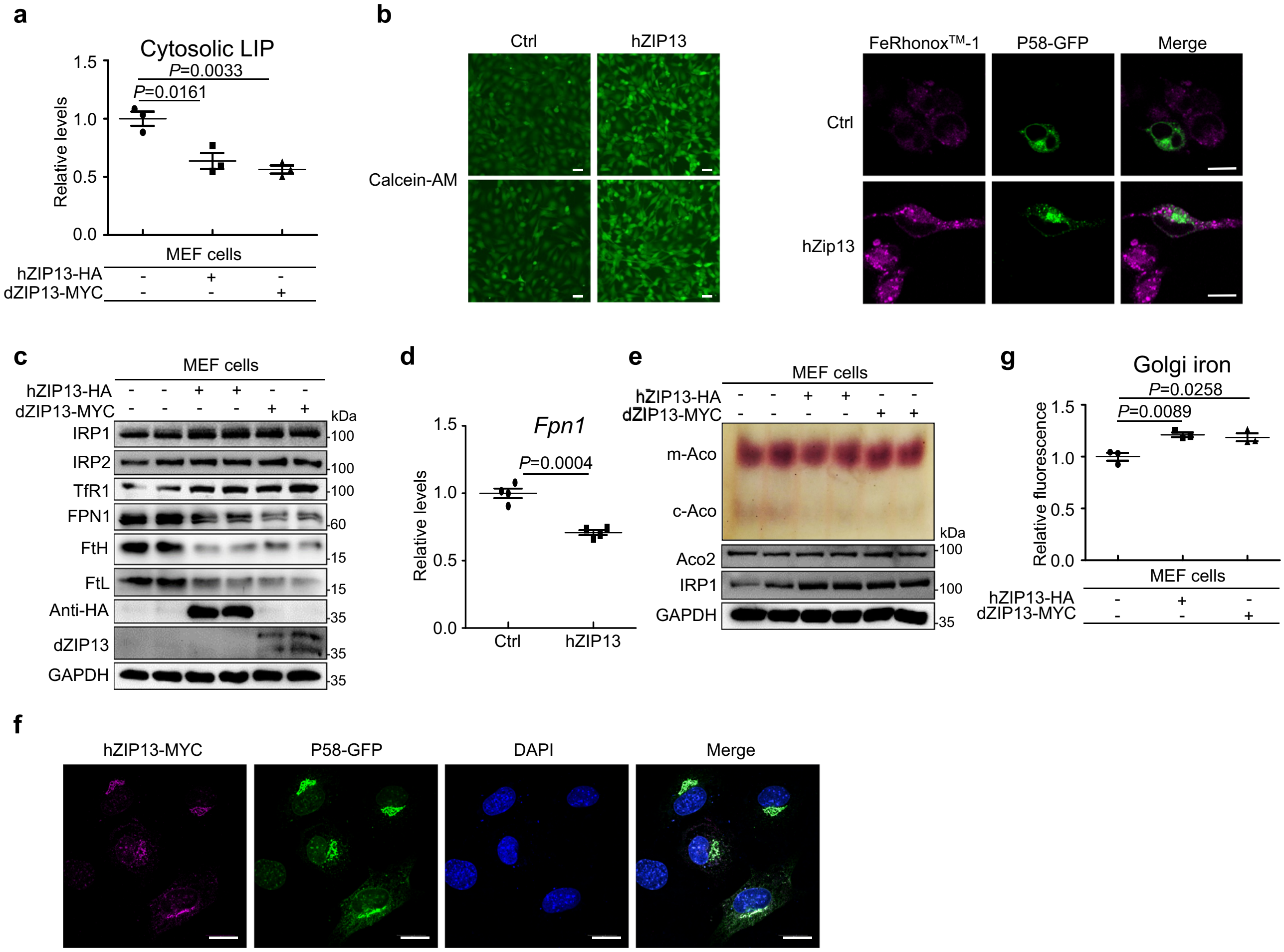

Fig. 1 | ZIP13 overexpression caused iron redistribution. a Cytosolic labile iron pool (LIP) in mouse embryonic fibroblasts (MEFs) indicated by Calcein-AM fluorescence (*n* = 3, biologically independent replicates). Ferrous iron quenches Calcein-AM fluorescence. LIP is indicated by fluorescence difference before and after deferiprone (DFP) treatment. **b** Cytosolic LIP and Golgi iron in MEFs indicated by Calcein-AM (green) and FeRhonox^{TM}-1 (magenta), respectively. Stronger fluorescence of Calcein-AM means reduced ferrous iron level. Golgi was marked by P58-GFP (green). Scale bar, 50 μm (Calcein-AM) or 20 μm (FeRhonox^{TM}-1). **c** Protein levels of IRP1, IRP2, TfR1, FPN1, FtH, FtL, hZIP13-HA, and dZIP13-MYC determined by immunoblotting. **d** The mRNA level of *Fpn1* was indicated by RT-qPCR (n = 4, biologically independent replicates). **e** A representative graph of in-gel assays of mitochondrial (m-Aco, encoded by *Aconitase2, Aco2*) and cytosolic (c-Aco, encoded by *Irp1*) aconitase in MEFs. **f** Immunofluorescence colocalization of exogenous hZIP13 (magenta) and Golgi marker P58 (green) in MEFs. DAPI: blue. Scale bar, 20 μm. **g** Levels of Golgi iron indicated by FeRhonox^{TM}-1 fluorescence (*n* = 3, biologically independent replicates). Each experiment at least was repeated independently three times with similar results (**c**–**e**). Data are mean ± SD. Statistical analysis was performed using two-tailed student's *t*-test (**a**–**g**). Source data are provided as a Source Data file.

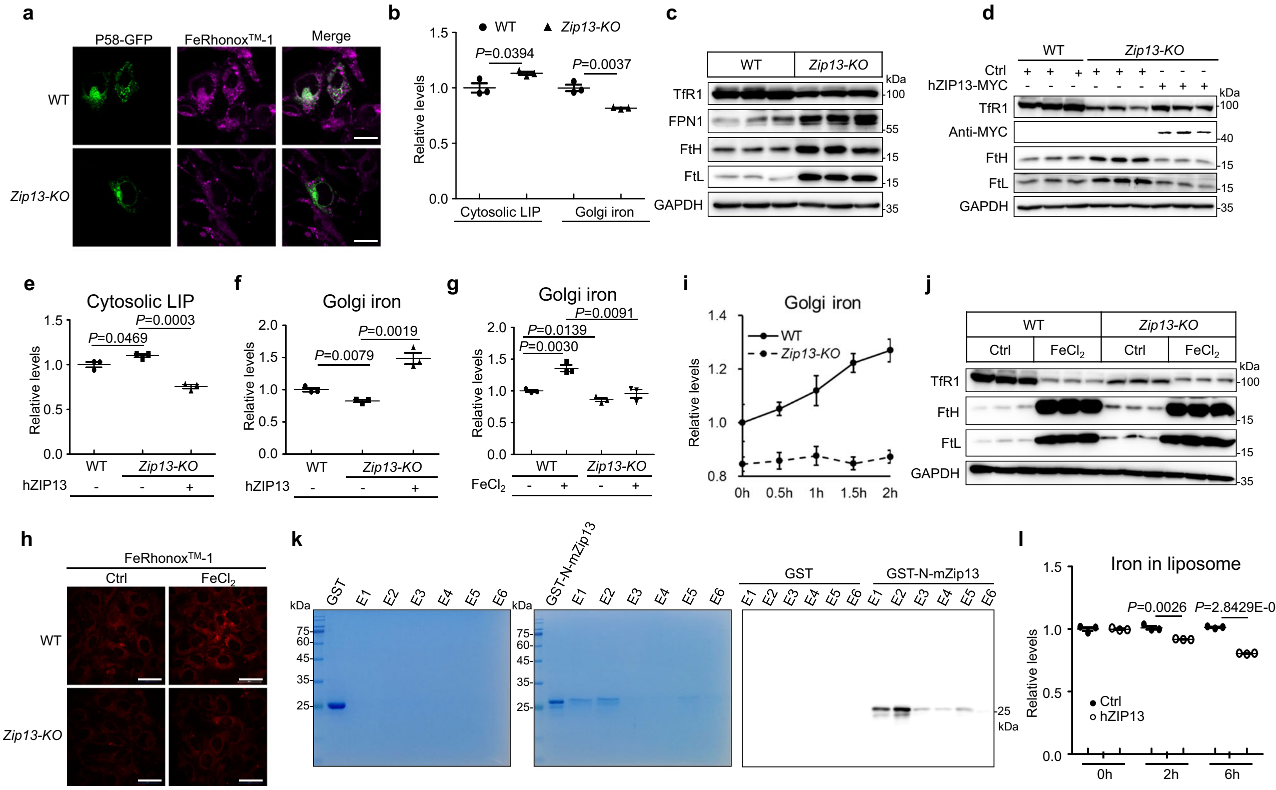

Fig. 2 | ZIP13 deficiency stopped iron trafficking from the cytosol to Golgi. **a** Levels of iron in Golgi. Iron stained by FeRhonox™-1(magenta), and Golgi marked by P58-GFP (green). Scale bar, 20 μm. **b** Levels of cytosolic LIP and Golgi iron measured in WT and *Zip13-KO* MEFs (Cytosolic LIP and Golgi iron: *n* = 3). **c** Protein levels of TfR1, FPN1, FtH, and FtL in WT and *Zip13-KO* MEFs. **d** The protein levels of TfR1, hZIP13-MYC, FtH, and FtL. **e**, **f** The levels of cytosolic LIP (**e**) and Golgi iron (**f**) in *Zip13-KO* MEFs after hZIP13 expression (n = 3). **g**, **h** Golgi iron of WT and *Zip13-KO* MEFs after treatment with 50 μM $FeCl_2$ for 24 h (**g**, *n* = 3). Scale bar, 50 μm. **i** A time course of iron transport from the cytosol to Golgi by WT and *Zip13-KO* MEFs (*n* = 3). WT and *Zip13-KO* MEFs were treated with 50 μM $FeCl_2$ for 0, 0.5, 1, 1.5, and 2 h, respectively, and then collected to detect the Golgi iron contents. **j** Protein levels of TfR1, FtH, and FtL in WT and *Zip13-KO* MEFs after with or without $FeCl_2$ treatment. **k** GST-N-mZIP13 and GST alone were tested for their abilities to bind Fe^{2+}. A Fe^{2+}-column (Fe^{2+} replacing Ni^{+}) was used. Elution was used to detect whether the protein could bind to Fe^{2+} by Commassie brilliant blue staining (left gel and middle gel) and western blotting (right gel). GST: GST protein, GST-N-mZIP13: fusion protein of mouse ZIP13 N-terminal and GST, E1-E6: eluates collected after passage through ferrous column. **l** Levels of iron ions were detected in the protein-free control and hZIP13-loaded liposomes at 0 h, 2 h, and 6 h, respectively, to verify the iron-transport activity of ZIP13 (*n* = 3). Iron levels were represented by relative changes of fluorescence signal (Calcein-Fe^{2+}). The "n" represents biologically independent replicates (**b**, **e**–**g**, **i**, and **l**). Each experiment was repeated independently at least three times with similar results (**c**, **d**, **j**, and **k**). Data are mean ± SD. Statistical analysis was performed using two-tailed student's *t*-test (**b**, **e**–**g**, and **l**). Source data are provided as a Source Data file.

much affected by ZIP13, implying that the amount of cytosolic iron exported through this avenue could likely be substantial.

ZIP13 loss stops the cytosolic iron flow to the ER/Golgi

To further understand the role of ZIP13 in the iron metabolism of mammalian cells, *Zip13* knockout (*Zip13-KO*) MEFs were generated from *Zip13*-mutant mice. The Golgi iron significantly decreased, while cytosolic LIP slightly increased (Fig. 2a, b, and Supplementary Fig. 1g). The decreased expression of TfR1 and increased expressions of FPN1, FtH, and FtL in *Zip13-KO* MEFs compared with WT consistently reflected the elevated cytosolic LIP (Fig. 2c). Given that no reliable and sensitive enough ZIP13 antibodies are available, we used tagged ZIP13 to follow mammalian ZIP13 expression. Expression of hZIP13 in *Zip13-KO* MEFs restored iron balance between the cytosol and ER/Golgi (Fig. 2d–f), indicating that the observed defects were indeed a result of ZIP13 loss and not due to an unrelated mutation. Similar results were confirmed with HeLa cells after knocking down *ZIP13* by RNAi (Supplementary Fig. 1h–j). To confirm the iron-transporting activity connected to ZIP13, we monitored the time course of ER/Golgi iron change when external iron was added. The ER/Golgi iron content in WT cells gradually increased after iron addition (Fig. 2g–i, and Supplementary Fig. 1k). However, in *Zip13-KO* cells no obvious alteration was noticed (Fig. 2g–i, and Supplementary Fig. 1k), suggesting ZIP13 is the sole, or at least by far the predominant, player involved in this transporting process. As a control, iron addition similarly increased cytosolic iron in *Zip13-KO* cells, as shown by the altered expression of TfR1, FtH, and FtL (Fig. 2j). These results were also confirmed with ICP-MS analyses using Golgi isolated from the livers of WT and *Zip13-KO* mice, which showed a substantial reduction of iron in the *Zip13-KO* Golgi (Supplementary Fig. 2a). Again, ZIP13 deficiency did not affect the mRNA levels of *Zip7*, *Zip8*, and *Zip14* (Supplementary Fig. 2b). The iron phenotype caused by ZIP13 deficiency could not be remedied by zinc addition or zinc chelation (Supplementary Fig. 2c, d).

The above described that at the cellular level, ZIP13 deficiency prevents iron transport from the cytosol to the secretory pathway. To further confirm that ZIP13 can directly transport iron, we first tested whether the extracellular portion of ZIP13 is able to bind iron. The N-terminal peptide of mouse ZIP13 (from 21aa to 67aa), when expressed after fusing to GST, could bind Fe^{2+}, but not avidly to Zn^{2+} (Fig. 2k, and Supplementary Fig. 2e). We also found that compared with the intact ZIP13, $ZIP13^{\Delta 21\text{-}67}$ (deleting 21-67 aa) expression only partially improved the iron phenotype of *Zip13-KO* MEFs (Supplementary Fig. 2f), suggesting that the iron-binding by this region is helpful for optimal iron transport related to ZIP13. We then used immunoaffinity-isolated tagged ZIP13 (ZIP13-HA) and reconstituted it into a liposome preparation (Supplementary Fig. 2g–l). The prepared liposome

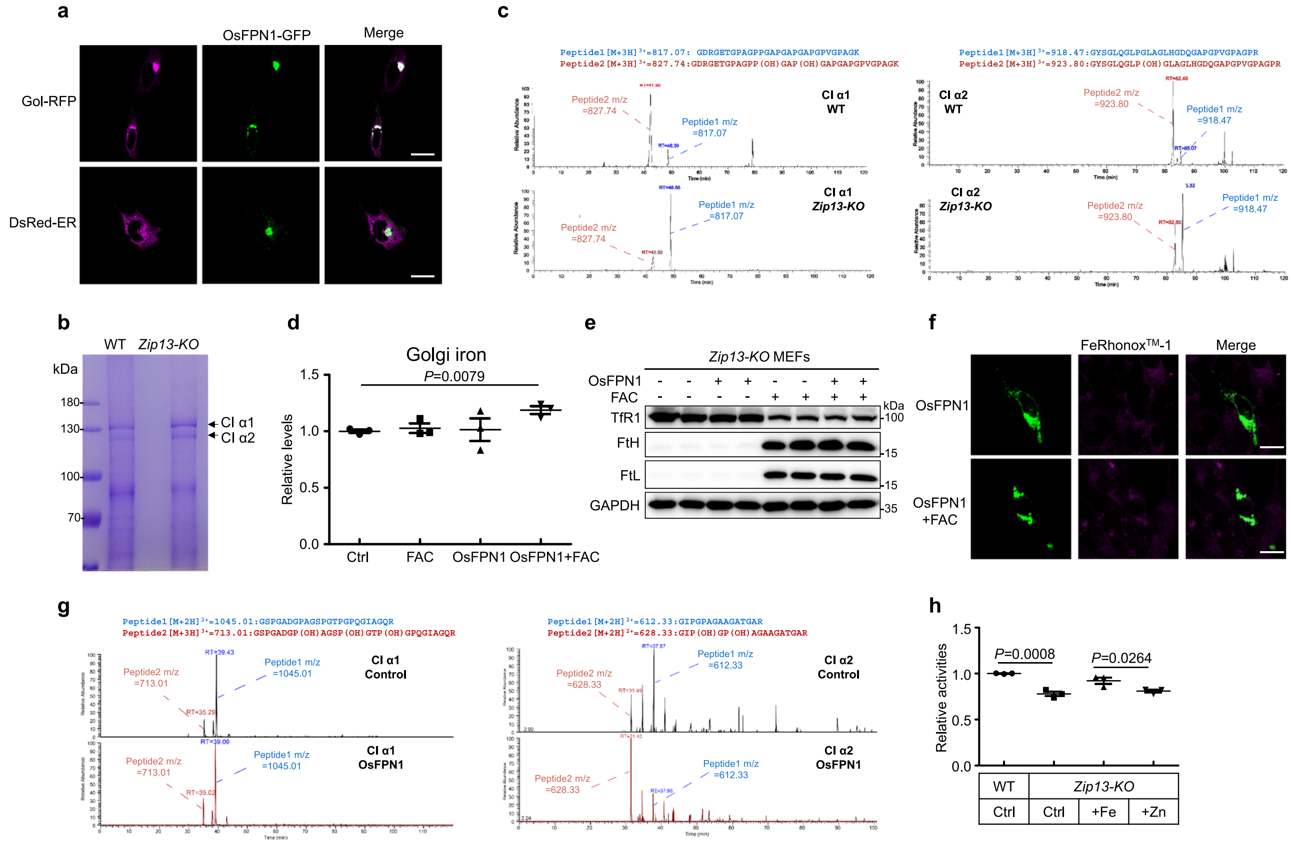

Fig. 3 | ZIP13 deficiency caused collagen hydroxylation deficiency that could be ameliorated by iron transport to ER/Golgi. a *Oryza sativa L* FPN1(OsFPN1) was mainly located at ER and Golgi. Magenta: ER (DsRed-ER) or Golgi (Gol-RFP), Green: OsFPN1-GFP. Scale bar, 20 μm. **b** Collagen was extracted from culture media, and then the α1 and α2 chains were separated by SDS-PAGE. CI α1: α1 chain of type I collagen, CI α2: α2 chain of type I collagen. **c** Levels of collagen hydroxylation measured by LC-MS. The peaks represent peptides corresponding to particular molecular weights. For a particular peptide, the hydroxylated and unhydroxylated forms have different molecular weights. Red: hydroxylation, Blue: nonhydroxylation. **d** The level of Golgi iron in *Zip13-KO* MEFs after OsFPN1 expression with 200 μM ferric ammonium citrate (FAC) incubation for 24 h. ($n = 3$, biologically independent replicates). **e** The expression of iron metabolism-related proteins in *Zip13-KO* MEFs after OsFPN1 expression, FAC treatment or OsFPN1 expression with FAC treatment. **f** The level of Golgi iron. Green: OsFPN1-GFP, Red: FeRhonox™-1. Scale bar, 20 μm. **g** Collagen hydroxylation in *Zip13-KO* MEFs with OsFPN1 and 200 μM FAC. **h** The activities of proline hydroxylase in the ER/Golgi isolated from WT and *Zip13-KO* cells were measured after the addition of iron or zinc ($n = 3$, biologically independent replicates). Each experiment was repeated independently at least three times with similar results (**a**–**e**). Data are mean ± SD. Statistical analysis was performed using two-tailed student's *t*-test (**d**–**h**). Source data are provided as a Source Data file.

exhibited apparent iron-transport activity in vitro (Fig. 2l, and Supplementary Fig. 2n). At the 2-h time point and more so at the 6-h time point, the enclosed iron levels were reduced (Fig. 2l). Together, these pieces of evidence indicated an inherent iron-transporting activity of ZIP13 in vitro. Notably, we also observed a zinc-transport activity of the constructed ZIP13 liposome (Supplementary Fig. 2m, n).

ER/Golgi-targeted FPN1 could partially substitute the function of ZIP13 loss

ZIP13 mutations in mammals present an overt phenotype of collagen under-crosslinking. For example, human with *ZIP13* mutations develop Ehlers-Danlos syndrome spondylodysplastic type 3 (EDSSPD3; OMIN #612350)[24,26,29], whose pathogenesis mechanism remains unresolved[14,25,26]. It is known that collagen hydroxylation is catalyzed by iron, oxygen, and vitamin C in the ER/Golgi[30–32]. To address whether this ZIP13-related phenotype is indeed related to iron, we tried to replenish the lost iron in the secretion pathway. The only known iron exporter is FPN1, which typically locates on the plasma membrane to export iron. We tried several versions of FPN1 construct and found OsFPN1-GFP (FPN1 homolog from *Oryza sativa L*, fused in frame to GFP), when expressed, well colocalized with the ER/Golgi, but not mitochondrion and lysosome (Fig. 3a, and Supplementary Fig. 3a)[33]. We then tested whether this mistargeted FPN1 could rescue the defective collagen hydroxylation associated with *ZIP13* loss. Type I collagen was extracted from the culture medium of WT and *Zip13-KO* MEFs, separated by SDS-PAGE gel (Fig. 3b), and analyzed by LC-MS. As reported before, the hydroxylation of prolyl residues in the α1 and α2 chains significantly reduced in *Zip13-KO* cells compared with WT, accompanied by a marked increase of non-hydroxylation of prolyl residues (Fig. 3c, and Supplementary Fig. 3b). Notably, with iron supplementation, expression of ER/Golgi-localized OsFPN1 could, to some extent, restore the iron level in the ER/Golgi to *Zip13-KO* MEFs, concomitant with significantly improved hydroxylation of the collagen (Fig. 3d-g, and Supplementary Fig. 3c). These results indicate that the collagen under-hydroxylation observed in ZIP13-deficient MEFs is due to an iron deficiency in the secretory pathway. Further, they suggest that the molecular functions of ZIP13 and FPN1 are analogous, only they reside on different cellular compartments leading to different cellular functions.

To more directly show that ER/Golgi iron deficiency underlies the inadequate collagen hydroxylation in *Zip13-KO* animals, we purified ER/Golgi from *Zip13-KO* cells and tested their hydroxylation activity. When normalized by the amount of total protein, the ER/Golgi extract from *Zip13-KO* cells indeed had reduced hydroxylation capability. Importantly, the addition of iron, but not zinc, could effectively rescue the compromised enzymatic activity (Fig. 3h), suggesting that

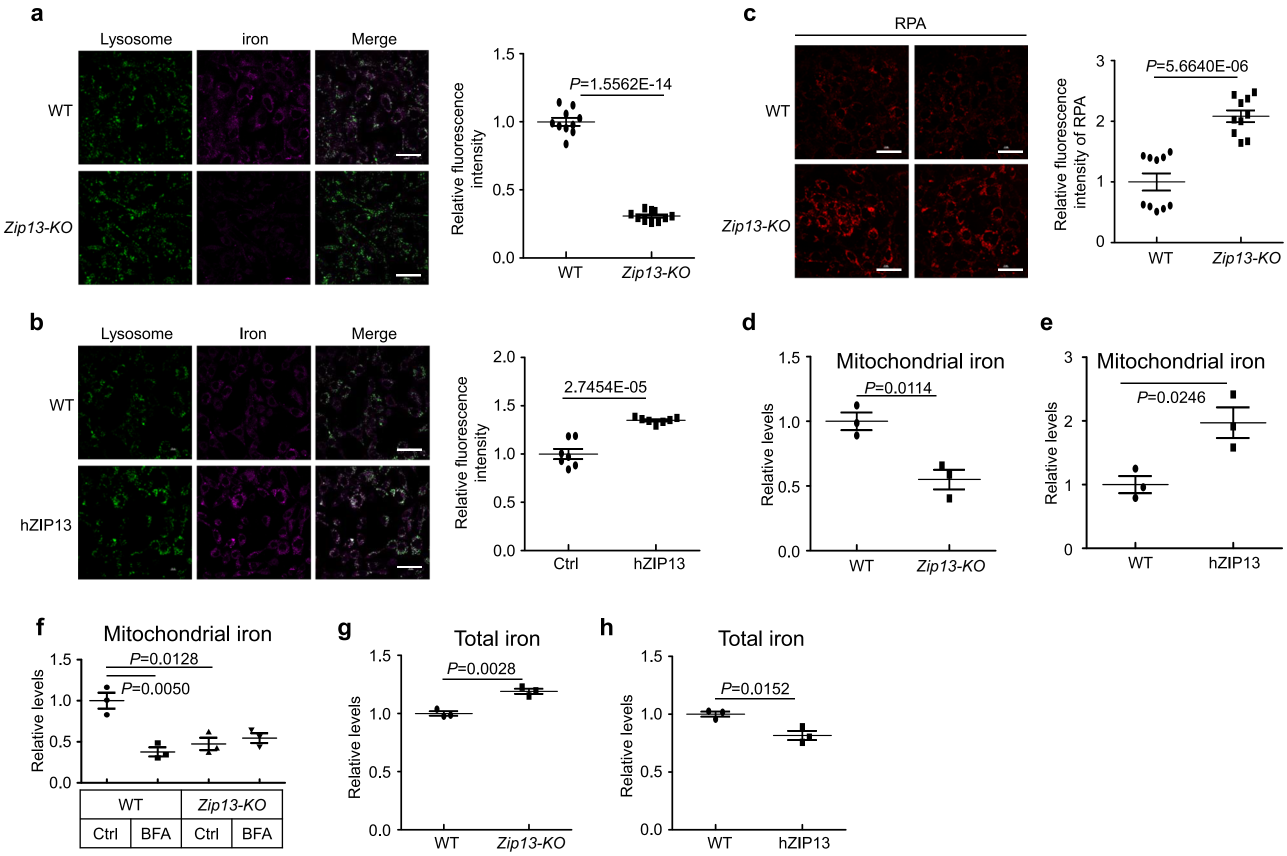

Fig. 4 | ZIP13 deficiency and overexpression affected the iron content of mitochondria and lysosome. a Levels of iron in lysosome of WT and *Zip13-KO* MEFs. Iron stained by iron probe, and lysosome marked by lysoTracker green DND-26 (left). Green: lysosome; Magenta: Iron. Scale bar, 50 µm. The level of lysosome iron was quantified (right) (*n* = 10, biologically independent replicates). **b** Levels of iron in lysosome of WT and hZIP13 overexpression MEFs. Green: lysosome; Magenta: Iron. Scale bar, 50 µm. The level of lysosome iron was quantified (right) (*n* = 7, biologically independent replicates). **c** Mitochondrial iron in WT and *Zip13-KO* MEFs indicated by Rhodamine B-[(1,10-phenanthroline-5-yl)-aminocarbonyl] benzyl ester (RPA). Ferrous iron quenches RPA fluorescence. The RPA fluorescence intensity is inversely proportional to the mitochondrial LIP. Scale bar, 50 µm. The fluorescence intensity was quantified (right) (*n* = 10, biologically independent replicates). **d**, **e** Mitochondrial iron in MEFs indicated by RPA. Iron is indicated by fluorescence difference before and after PIH treatment (*n* = 3, biologically independent replicates). **f** Mitochondrial iron were detected in WT and *Zip13-KO* MEFs after treated with or without 50 µM brefeldin A (BFA) for 6 h (*n* = 3, biologically independent replicates). **g** Levels of total iron in WT and *Zip13-KO* MEFs were indicated by ICP-MS (*n* = 3, biologically independent replicates). **h** Levels of total iron in WT and hZIP13 overexpression MEFs (*n* = 4, biologically independent replicates). Data are mean ± SD. Statistical analysis was performed using two-tailed student's *t*-test (**a**–**h**). Source data are provided as a Source Data file.

disruption of iron homeostasis is physiologically closely relevant to the collagen phenotypes observed in *Zip13-KO* mice.

ZIP13 modulation additionally affects the iron homeostasis in lysosomes and mitochondria

The classical secretion pathway is the corridor where the contents are sorted out and some get secreted. We next asked whether the ER/Golgi iron promoted by ZIP13 reached any other destination. We first examined whether lysosomal iron would be affected when ZIP13 expression is modulated. Interestingly, the iron level in the lysosome significantly decreased upon ZIP13 loss (Fig. 4a). This is not likely a result of cytosolic iron alteration since cytosolic iron was elevated when ZIP13 was suppressed. Therefore, an iron deficiency in the ER/Golgi leads to iron shortage in the lysosomal compartment. When ZIP13 was overexpressed, lysosomal iron content increased (Fig. 4b). We next analyzed mitochondrial iron. To our surprise, we saw obviously enhanced labile iron in ZIP13-overexpression cells and iron deficiency in *Zip13*-knockout cells (Fig. 4c–e), similar to what was observed in the lysosome. Again, this cannot be explained by cytosolic iron level change as ZIP13 overexpression and loss would respectively downregulate and upregulate cytosolic iron levels. We conclude that ER/Golgi iron deficiency also results in mitochondrial iron deficiency.

It is well established in cell biology that ER/Golgi transport some of their contents to the lysosome. Recently it has also been demonstrated that there exists ER/mitochondria contact where calcium and zinc can be transported directly from the ER to mitochondria[34,35]. It is not investigated, however, how iron can be imparted to the mitochondria from the ER. We speculated that iron might behave like calcium and zinc in the sense that they could all transfer from the ER to the mitochondria, or alternatively, iron could transfer via lysosome to the mitochondria, considering that iron transfer between lysosome and mitochondria has been reported, likely via a kiss-and run mechanism[4]. According to the first model, if iron transport gets blocked after the ER, mitochondrial iron loading from the ER would be expected not to be affected; in contrast, according to the second scenario, ER iron would not find its way to the mitochondrion. To put these thoughts to the test, WT and *Zip13-KO* MEFs were treated with Brefeldin A (BFA), a chemical inhibitor of the conventional ER-Golgi transport pathway. In WT MEF cells, BFA significantly decreased iron flow to the mitochondria, suggesting the second scenario may be correct. In *Zip13-KO* MEFs, since ER/Golgi lacks iron, BFA had no

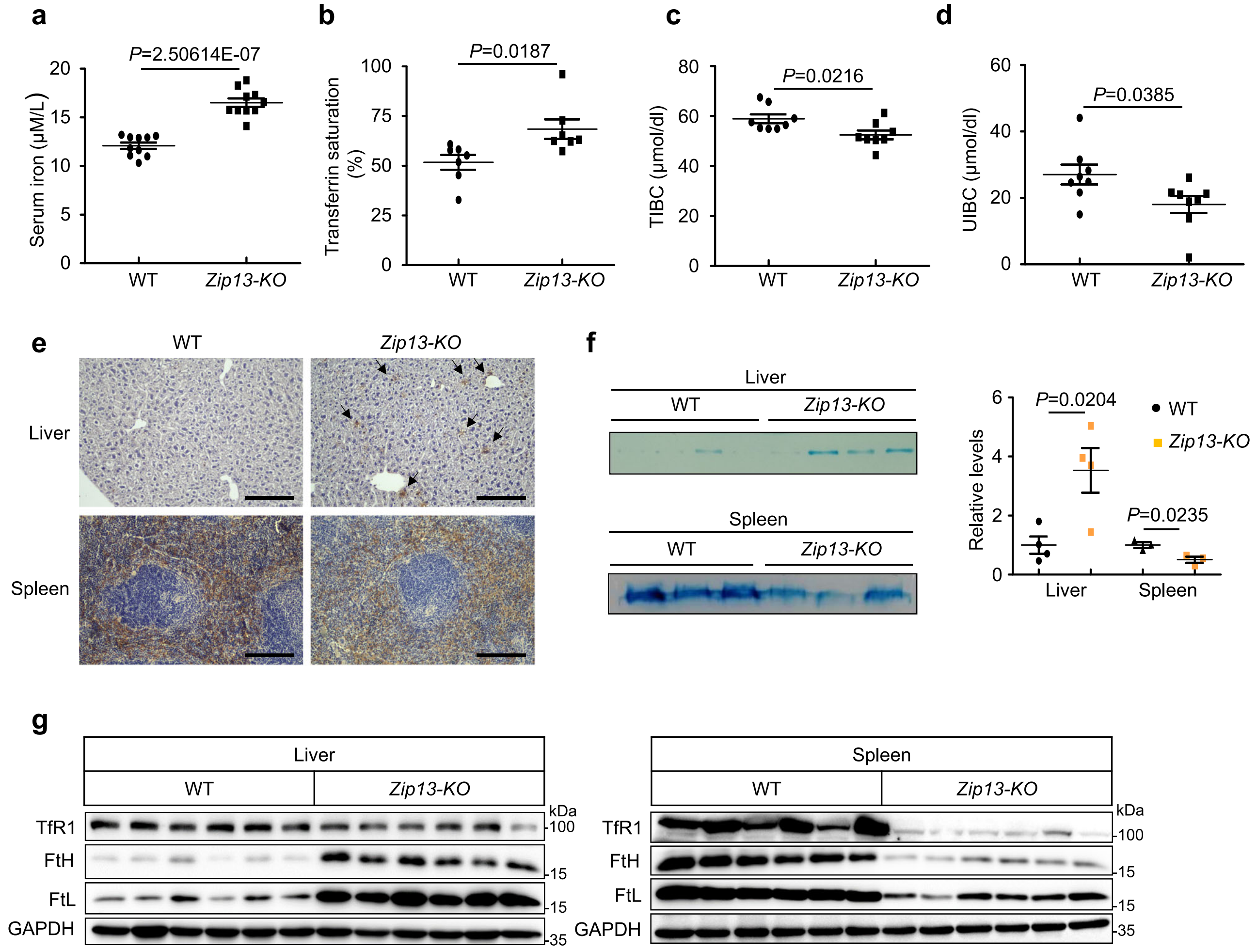

Fig. 5 | ZIP13 deficiency led to iron metabolism abnormalities. a Levels of serum iron in WT and *Zip13-KO* mice (*n* = 10, biologically independent replicates). **b** Transferrin saturations in the serum of WT and *Zip13-KO* mice (*n* = 7, biologically independent replicates). **c** The total iron binding capacity (total iron binding capacity, TIBC) of the serum (*n* = 8, biologically independent replicates). **d** The unsaturated iron-binding capacity (unsaturated iron binding capacity, UIBC) of the serum (*n* = 8, biologically independent replicates). **e** Iron in the liver and spleen of WT and *Zip13-KO* mice detected by DAB-enhanced Perls' staining (brown). Arrows indicate iron stains in the liver. Scale bar, 200 μm. **f** Staining of ferric iron (bound to ferritin) with native PAGE gel (left). Quantification of Fig. 5f (right) (liver, *n* = 4; spleen, *n* = 3; biologically independent replicates). **g** Protein levels of TfR1, FtH, and FtL in the liver and spleen of WT and *Zip13-KO* mice (*n* = 6, biologically independent replicates). Data are mean ± SD. Statistical analysis was performed using two-tailed student's *t*-test (**a**–**d**, **f**). Source data are provided as a Source Data file.

appreciable effects on the mitochondrial iron level (Fig. 4f). This is an important control because it argues against the possibility that BFA could have disrupted another unrelated cellular process that might affect mitochondrial iron loading.

Another interesting question to ask is whether the iron in the secretory pathway could be secreted outwards. As stated, in the fly, iron is carried by ferritin in the secretory compartment to the hemolymph. In contrast, mammalian ferritins have no classical secretion signals and are not found in the ER/Golgi. Surprisingly, in ZIP13-deficient cells, the total iron level increased, meaning the overall iron export activity was impaired (Fig. 4g), although cytosolic iron accumulation was accompanied by a compromised expression of iron uptake proteins and increased FPN1 expression. Conversely, in ZIP13-overexpression cells, total iron significantly decreased, indicating that more iron was exported than in the control cells (Fig. 4h). These results imply that a fraction of the iron finds its way out via the classical secretion pathway. In summary, ZIP13 mediates iron trafficking from the cytosol to the ER/Golgi and multiple downstream organelles and likely even to the extracellular space. We do not know, however, whether the possible iron outflow is through the Golgi or other routes, such as the lysosome.

ZIP13 loss results in iron dyshomeostasis in vivo

Previous work has reported that ZIP13 deficiency causes significant bone and connective tissue development disorder[26,29,36]. We confirmed that *Zip13* knockout mice indeed displayed growth retardation, tooth deformity, and progressive kyphosis (Supplementary Fig. 4a, b). These defects could not be rescued by intraperitoneal injection of iron-dextran (Supplementary Fig. 4c), although serum iron levels had been effectively augmented (Supplementary Fig. 4d). This is consistent with our above observation from the cell culture studies that additional iron failed to get into the ER/Golgi compartment without ZIP13.

Besides the significantly reduced collagen content in tissues such as heart, liver, lung, kidney, intestine, and skin (Supplementary Fig. 4e), serum iron and transferrin saturation evidently increased in *Zip13-KO* mice compared with WT (Fig. 5a, b, and Supplementary Fig. 4d). The serum total iron binding capacity (TIBC) and unsaturated iron binding capacity (UIBC) of *Zip13-KO* mice slightly but significantly dropped (Fig. 5c, d). Surprisingly, overall hematological abnormality in *Zip13-KO* mice was very mild, with only a little reduction in the mean corpusular volume (MCV) value (Supplementary Fig. 5a–f). Iron contents in various tissues of mice were

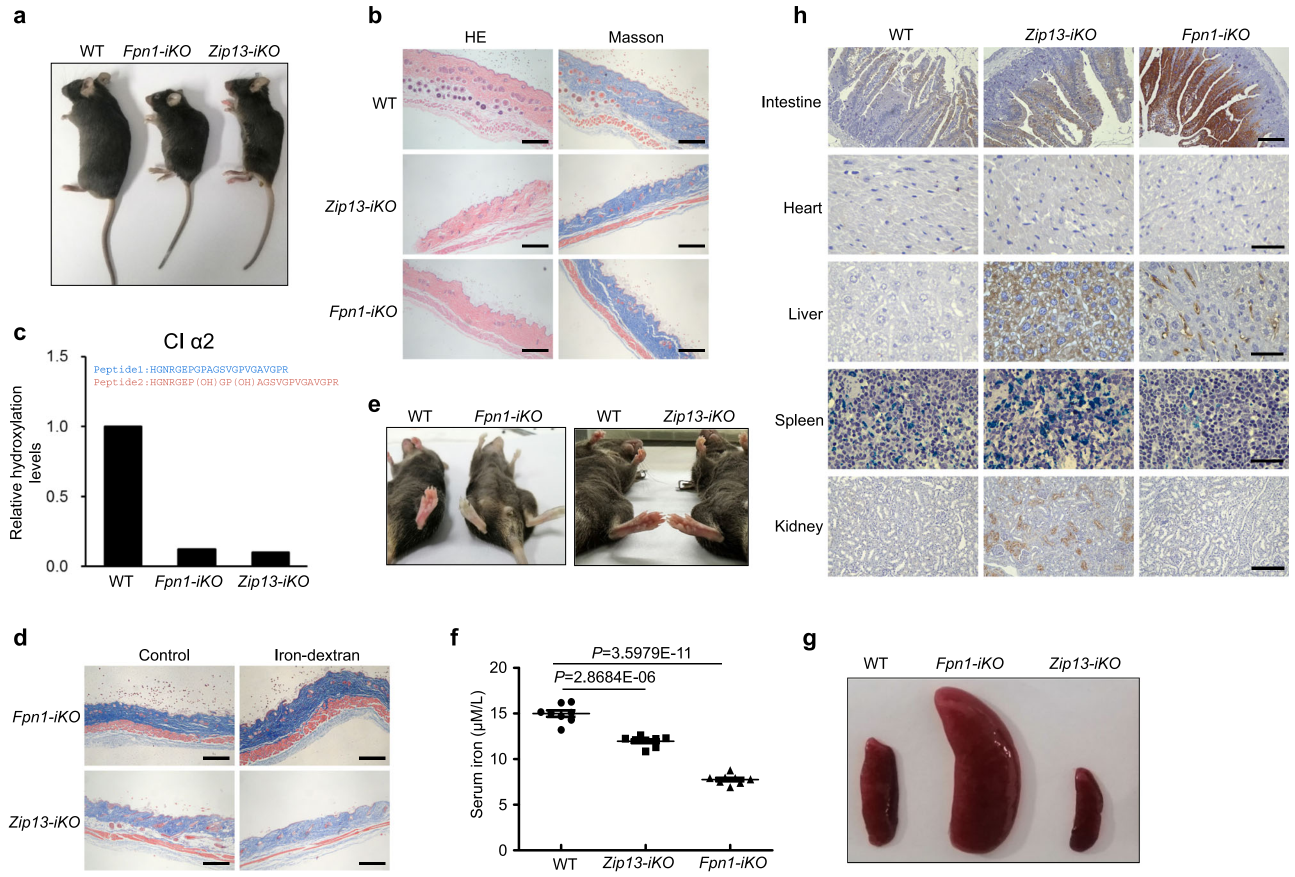

Fig. 6 | Inducible losses of FPN1 and ZIP13 resulted in strong and distinctive iron dyshomeostasis patterns. a *Fpn1-iKO* and *Zip13-iKO* mice displayed similar hunchback symptoms. **b** HE (left) and Masson (right, blue) staining of mouse skins. Scale bar, 200 µm. **c** Levels of collagen hydroxylation were measured by LC-MS. The ratios of collagen hydroxylation to nonhydroxylation relative to that of WT were shown. **d** Iron supplementation increased the collage thickness of the skin in *Fpn1-iKO* mice, but not in *Zip13-iKO* mice (blue). Scale bar, 200 µm. **e** *Fpn1-iKO* mice were pale and bloodless, but *Zip13-iKO* mice were not. **f** Levels of serum iron in WT, *Fpn1-iKO*, and *Zip13-iKO* mice ($n = 8$, biologically independent replicates). **g** Spleens of WT, *Fpn1-iKO*, and *Zip13-iKO* mice. **h**, Perls' staining of some tissues in WT, *Fpn1-iKO*, and *Zip13-iKO* mice. Intestine, heart, liver, and kidney: brown; Spleen: blue. Scale bar, 200 µm. Each experiment was repeated independently at least three times with similar results (**b**–**h**). Data are mean ± SD. Statistical analysis was performed using two-tailed student's *t*-test (**f**). Source data are provided as a Source Data file.

analyzed to thoroughly examine the possible effects of *Zip13* deletion on iron metabolism (Supplementary Fig. 6a–j). Iron accumulation in the liver and deficiency in the spleen and stomach of *Zip13-KO* mice were noticed (Supplementary Fig. 6b, c, and g). Histochemical Perls' iron staining and native in-gel ferritin iron staining further confirmed these (Fig. 5e, f), which were further substantiated by Western blot and immunohistochemistry analyses of the expressions of TfR1, FPN1, FtH, and FtL (Fig. 5g, and Supplementary Fig. 7). The increase of aspartate aminotransferase (AST) in the serum of *Zip13-KO* mice indicated liver damage (Supplementary Fig. 8a). No obvious alterations for the other biochemical indices such as alanine aminotransferase (ALT), creatine kinase (CK), creatinine (CREA), and lactate dehydrogenase (LDH) were observed except for triglyceride (TG), which markedly decreased (Supplementary Fig. 8b–f).

The serum ferritin level is often used clinically to judge body iron storage[37–39]. We, therefore, measured the serum ferritin content of WT and *Zip13-KO* mice with or without iron treatment. With the iron injection, the levels of FtH and FtL in the serum of WT and *Zip13-KO* mice both increased (Supplementary Fig. 8g, h), but the level of FtH was significantly higher in the serum of *Zip13-KO* mice than that of WT mice, with or without iron injection (Supplementary Fig. 8h). These results clearly indicate that ZIP13 is involved in iron homeostasis in vivo.

The inducible loss of FPN1 and ZIP13 results in drastically differential iron dyshomeostasis patterns

Now it becomes apparent that FPN1 and ZIP13 help remove the cytosolic iron via two parallel pathways: one directly outward cross the plasma membrane and the other entering the secretion pathway. We then tried to compare their functions in iron homeostasis. Individual germline mutants of both ZIP13 and FPN1 are associated with severe developmental abnormalities[26,40]. To bypass their early developmental problems and explore their individual functions post-development, we generated inducible knockout (iKO) of *Fpn1* or *Zip13* mice by injecting tamoxifen into corresponding pre-pubertal *R26*^{CreERT2}; *Fpn1* $^{fl/fl}$ (*Fpn1-iKO*) or *R26*^{CreERT2}; *Zip13* $^{fl/fl}$ (*Zip13-iKO*) mice. Two months after induction, *Fpn1-iKO* mice exhibited similar symptoms of skin relaxation and kyphosis, characteristic of *Zip13-iKO* mice (Fig. 6a). Masson staining revealed that the collagen contents in the skin of *Fpn1-iKO* and *Zip13-iKO* mice both noticeably decreased (Fig. 6b). When we extracted the collagen from the skin of these mice and analyzed it with LC-MS (Supplementary Fig. 9a), the hydroxylation levels of collagen were indeed markedly decreased in the skin of both *Fpn1-iKO* and *Zip13-iKO* mice (Fig. 6c, and Supplementary Fig. 9b). We speculated that the decrease of collagen synthesis in the skin of *Fpn1-iKO* mice might be secondary to systemic iron deficiency, that is, severe iron deficiency in the cytosol might cause a secondary iron shortage in the secretory compartments. To test this possibility, *Fpn1-iKO* mice were injected

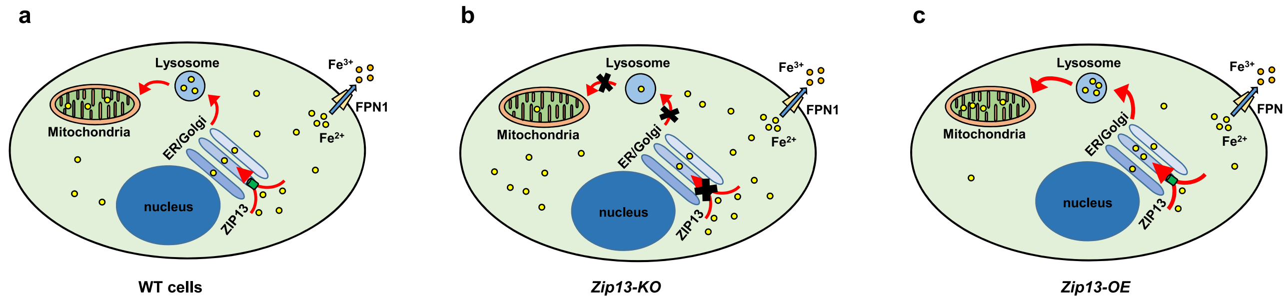

Fig. 7 | A schematic model depicting ZIP13's role in iron homeostasis regulation. ZIP13 plays a critical role in gating an iron flow route that affects iron homeostasis in several major cellular compartments, including the cytosol, the ER/Golgi, the lysosome as well as the mitochondrion. **a** Under normal conditions, ZIP13 redistributes or partitions the cytosolic iron. It transports a part of the cytosolic iron into the ER/Golgi, where it traffics further to the lysosome and mitochondria. **b** When ZIP13 loses its function, this iron trafficking route is blocked. More iron is accumulated in the cytosol and less in the ER/Golgi, lysosome, and mitochondrion. **c** When ZIP13 is more active, more cytosolic iron is diverted to this pathway, leading to more iron in the corresponding compartments and less iron in the cytosol. Green: ZIP13; yellow: Fe^{2+}; orange: Fe^{3+}; pink: FPN1.

intraperitoneally with iron-dextran to increase the systemic iron content (Supplementary Fig. 9c). Amazingly, the collagen content in the skin significantly improved (Fig. 6d), in contrast to our rescue with iron-dextran in the *Zip13-KO* mice. These results corroborate the hypothesis that iron deficiency (in ER/Golgi) underlies the decrease of collagen synthesis in both *Zip13-iKO* and *Fpn1-iKO* mice.

Fpn1-iKO mice were pale with severe anemia symptoms, while *Zip13-iKO* mice were not anemic (Fig. 6e). Routine blood test showed that the amounts of white blood cell (WBC), lymphocyte, and monocyte of *Fpn1-iKO* mice significantly increased (Supplementary Fig. 10a–c), while those of red blood cell (RBC), hemoglobin (HGB), hematocrit (HCT), and MCV obviously decreased (Supplementary Fig. 10d–g). The levels of mean corpuscular hemoglobin (MCH) and mean corpuscular hemoglobin concentration (MHCH) also increased in the *Fpn1-iKO* mice (Supplementary Fig. 10h, i). Like *Zip13-KO* mice, *Zip13-iKO* mice had little overt hematological abnormality (Supplementary Fig. 10a–i), although *Zip13-iKO* mice were also low in serum iron (Fig. 6f). The spleen of *Fpn1-iKO* mouse was abnormally enlarged, while that of the *Zip13-iKO* mouse was smaller (Fig. 6g). However, when taking the body size into account, the smaller *Zip13-iKO* spleen appears insignificant as compared to that of the WT.

Before we further analyzed possible iron dyshomeostasis in other tissues, we estimated the gene knockout efficiency of *Zip13* and *Fpn1* (Supplementary Fig. 11a–j). Every tissue examined had roughly comparable deletion efficiencies for *Zip13-iKO* and *Fpn1-iKO*. The intestine, spleen, and liver were among the tissues where *Zip13* or *Fpn1* was most effectively removed (Supplementary Fig. 11a–f). The iron levels in the hearts of both *Fpn1-iKO* and *Zip13-iKO* mice were decreased (Supplementary Fig. 12a). Moreover, the level of iron in the spleen was significantly reduced in *Fpn1-iKO* mice, whereas it increased in *Zip13-iKO* mice (Fig. 6h, and Supplementary Fig. 12b). Consistently, Western blot analyses confirmed an array of abnormal expression patterns of iron metabolism-related proteins in the heart, liver, spleen, and kidney of *Fpn1-iKO* and *Zip13-iKO* mice (Supplementary Fig. 12f–j). The levels of FtH and FtL were also obviously elevated in the serum of *Fpn1-iKO* and *Zip13-iKO* mice (Supplementary Fig. 12k–m).

Histology analyses revealed more strikingly different iron dyshomeostasis patterns between *Fpn1-iKO* and *Zip13-iKO* mice. In the liver, while both *Fpn1-iKO* and *Zip13-iKO* mice had elevated iron levels, *Fpn1* deletion caused iron accumulation primarily in the macrophage, whereas *Zip13* deletion led to almost ubiquitous iron accumulation in the hepatocyte (Fig. 6h, and Supplementary Fig. 12c). In intestinal epithelial cells, evident iron deposition was observed only for *Fpn1* mutant but not for the *Zip13* deletion (Fig. 6h, and Supplementary Fig. 12d). In the spleen, pronounced iron accumulation was seen in spleen macrophages of *Zip13-iKO* mice (Fig. 6h). Strikingly, iron deposition was also noticed in the renal tubular cells in *Zip13-iKO* mice (Fig. 6h, and Supplementary Fig. 12e), a region where iron reabsorption is suspected[11,41–43] Therefore, mutations of *Fpn1* and *Zip13* both result in iron accumulation, but they appear to function mainly in a non-overlapping manner at different body regions. Induced deletion of *Zip13* in vivo leads to widespread iron deposition in multiple tissues.

Discussion

Intracellular iron trafficking is a relatively poorly understood process. Our studies here uncovered an unexpected iron route. ZIP13 gates the iron flow to the ER/Golgi apparatus, which serves as a hub for the iron to reach multiple cellular destinations (Fig. 7). ZIP13 loss affects virtually all major intracellular compartments examined, which include the cytosol, the ER/Golgi, the lysosome, and the mitochondrion. This knowledge helps bridge our understanding of individual organellar iron homeostasis. The vital role of ZIP13 also justifies its broad expression. It helps answer our initial puzzle that even if ZIP13 supplies iron for the cofactor of collagen crosslinking, it is also in many other cell types that appear not to be synthesizing and secreting collagen.

The collagen under-hydroxylation etiology of EDSSPD3 has been controversial and mysterious before this work[14]. The revelation of mammalian ZIP13 promoting iron export to the ER/Golgi suggests that lack of iron underlies the defect of EDSSPD3. Indeed, we have shown here that systemic lack of iron, induced by Fpn1 loss, similarly resulted in skin defects; restoration of iron to the secretory compartment in ZIP13-loss cells significantly improved collagen hydroxylation. Another puzzling issue could also find its answer here; it was found previously that in EDSSPD3 patients, when their fibroblast extracts were tested for lysyl- and prolyl-hydroxylase activities, they were normal[29]. The discrepancy of reduced hydroxylation of collagens and the in vitro normal lysyl hydroxylase and prolyl hydroxylase activities could be well explained by our current findings: ZIP13 loss led to a decreased iron content in the ER/Golgi, resulting in the loss of iron cofactor for ER-resident lysine and proline hydroxylation enzymes. However, this regional iron deficiency would not be reproduced with cell extract plus assaying buffer (which contains exogenously added iron). In other words, the fibroblast extract may not be iron deficient even though the ER/Golgi is; in addition, enzymatic activity is assayed in the assaying buffer, which has to contain a reasonable amount of iron. These external iron neutralized or covered the original ER/Golgi iron deficiency occurring in vivo.

Because ZIP proteins are typically zinc (metal) importers (moving zinc towards the cytosol), it is intriguing that ZIP13 facillitates iron export by moving iron from the cytosol to the secretory pathway. The zinc transporting activity of ZIP13 has been noticed before[15,17,23–26], but in the fly we found that the primary physiological function of ZIP13 is iron instead of zinc[17]. The ability of ZIP13 to transport zinc or iron is not contradictory. Promiscuity has been reported for some other metal transporters. For example, DMT1 has been shown to be able to transport multiple metals but its primary in vivo function is iron[44,45]. ZIP14 was found to transport iron but later revealed that under normal physiological states its function is mainly to transport manganese[46,47], and only when iron is in surplus, it is involved in liver iron accumulation[48]. We have demonstrated before that within the transmembrane 4 of dZIP13, an evolutionarily absolutely conserved DNXXH motif, differing from the HNXXD motif in the other ZIPs, is responsible for its iron activity in *Drosophila*[15]. Interestingly, structural studies have revealed a binuclear metal center in the ZIP transport pathway[49]. Recently, it has been further shown that in the transmembrane domain of ZupT, an *E. coli* member of the ZIP transporter family, one metal-binding site binds zinc, cadmium, and iron, while the other binds iron only[50]. It is obvious that much more work awaits to explain how ZIP proteins work and how ZIP13 has this unique property.

We noticed that in some tissues, *Zip13-iKO* mice tend to have more pronounced iron accumulation than *Zip13-KO* mice. We suspect this is due to a compensatory action during early development for germline knockout mutants. It is known that embryonic cells are more flexible or totipotent at the early stage of development and can be reprogramed in different ways. At later stages, the epigenetic program is more fixed, and cells become less adaptable to external cues or changes. This appears to be the case in many situations[51]. Therefore, we believe that the native roles of ZIP13 in iron homeostasis could be more faithfully reflected by the inducible knockout of ZIP13 post the early developmental stage. Given that incomplete removal of the gene was observed in some tissues, it is conceivable that ZIP13's physiological roles in organismal iron homeostasis may be even more prominent than what we reported here.

While both FPN1 and ZIP13 loss lead to iron accumulation in the cell, their functions seem not redundant. In fact, the types of cells affected by their losses are largely non-overlapping. *Fpn1* deletion caused iron accumulation in the liver macrophages and intestinal epithelial cells, but *Zip13* deletion led to iron accumulation in the hepatocytes, spleen macrophages, and renal tubular cells. One provocative thought is that FPN1 exists mainly to provide iron for the blood formation. Loss of FPN1 affects regions, including the intestine, for iron absorption, and macrophages for iron recycling. Along this line of thinking, it is no wonder that there is no apparent FPN1 homolog in *Drosophila* because the fly has no RBCs. However, ZIP13 is indispensable because all metazoans need an iron trafficking avenue along the secretory pathway for cytosolic iron detoxification, collagen formation/maturation, and the iron procurement of multiple intracellular compartments. In summary, we have uncovered an essential protein that is reuired for iron transport to ER/Golgi, which opens the window for further research to fully comprehend its physiological significance and molecular details against the backdrop of an already complex network of iron homeostasis.

Methods

Animals

Zip13$^{+/-}$, *Zip13* $^{flox/flox}$ and hZIP13-HA mice on C57BL/6 N background were purchased from Cyagen (Suzhou, China). Schemes of generating these mice were detailed in the Supplementary data, as provided by the company (Supplementary Fig. 2g, 3d, e). The wild-type (WT) and *Zip13*$^{-/-}$ (*Zip13-KO*) mice were obtained by self-crossing the *Zip13*$^{+/-}$ mice. The 2 months old WT and *Zip13*$^{-/-}$ male mice were used for the experiments. *Fpn1*$^{flox/flox}$ mice on 129/SvEvTac background were originated from Nancy Andrews' lab (Jackson lab, Strain #: 017790). To obtain mice on C57BL/6 N background, *Fpn1*$^{flox/flox}$ mice were crossed with C57BL/6 N WT mice for ten generations. *Fpn1*$^{flox/flox}$ and *Zip13*$^{flox/flox}$ mice were crossed with *R26*^{CreERT2} mice on C57BL/6 N background to generate *Cre*$^{+/+}$*Fpn1*$^{flox/flox}$ and *Cre*$^{+/+}$*Zip13*$^{flox/flox}$ mice, respectively. These mice carry a tamoxifen-inducible Cre recombinase under the control of the *Rosa26* (R26) promoter.

To induce gene knockout, 1 month old *Cre*$^{+/+}$*Zip13*$^{flox/flox}$ and *Cre*$^{+/+}$*Fpn1*$^{flox/flox}$ male mice were injected intraperitoneally with tamoxifen (100 mg/kg, MedChemExpress, Shanghai, China) for 7 consecutive days to active Cre recombinase and kept for 2 months before sacrifice. Tamoxifen was dissolved in corn oil (Merck-millipore, Darmstadt, Germany) at concentrations 20 mg/ml. 100 µl tamoxifen solution or corn oil was injected intraperitoneally. All mice were housed in the specific pathogen-free (SPF) room under controlled temperature (20-26°C) and humidity (40–70%) conditions with 12 h light/dark cycle. The mice were fed a standard rodent pellet diet (containing 113.70 mg/kg iron and 31.60 mg/kg zinc). The gene knock-out efficiency of *Zip13* and *Fpn1* induced by tamoxifen was detected by qPCR using genomic DNA as templates. The primer sequences were provided in Supplementary Table 1 and Supplementary Table 2 in the Supplementary information. Because estrogen might interfere with the experimental results in female mice, male mice were used for research in this study. Sample size for each experiment was indicated in the figure legends (minimum of $n = 3$, mostly $n = 7$–10 mice per group). All procedures were carried out according to the NIH Guide for the Care and Use of Laboratory Animals and were approved by the Animal Experimentation Administration of Shenzhen Institutes of Advanced Technology, Chinese Academy of Sciences (Approval number: SIAT-IACUC-200405-HCS-LHH-A1022-01).

Iron treatment of animals

One month old WT and *Zip13-KO* male mice were administered intraperitoneally with 50 mg/kg, 100 mg/kg, and 300 mg/kg iron-dextran (Merck-millipore, cat# D8517-100 ml) twice a week for 1 month, respectively. The same volume of 0.9% NaCl was administered as the vehicle control. Following each treatment, blood and tissues were harvested for iron content detection.

Preparation of mouse MEF cell line

Primary MEFs were isolated from E12.5 pregnant *Zip13*$^{+/-}$ mice. MEFs were cultured in DMEM medium with 10% fetal bovine serum, 4 mM glutamine, 100 U/ml penicillin, 100 µg/ml streptomycin, 55 µM β-mercaptoethanol, and 1× Non-essential amino acids. Primary MEFs were plated into a 6-well dish and cultured overnight, and then transfected with the SV40 large T antigen. When the cells were just confluent, they were split into 10 cm dishes. Subsequently, these cells were passaged at least five times with a 1/10 ratio. Genotypes were identified by PCR.

Cell culture and transfection

HeLa cells was a gift from Prof. Kuanyu Li Lab (Nanjing University, China). For transfection, Lipofectamine™3000 transfection reagent (Thermo Fisher Scientific, Inc., Waltham, MA, cat# L3000015) was used according to the supplier's manual. Transfected plasmids included pCDNA3.1-hZIP13-MYC, pCDNA3.1-hZIP13-HA, p58-GFP, pIRESeno-dZIP13-MYC, pCDNA3.1-hZIP7-GFP, and pIRESeno-Catsup-flag. Cells were harvested 24 h post transfection for further analysis. HeLa cells were transfected with shRNAc, purchased from FulenGen (Guangzhou, China, cat# HSH064525), targeting *ZIP13*. Control shRNA target sequence: GCTTCGCGCCGTAGTCTTA. Human ZIP13 shRNAc target sequence: GCTGTGATTCCGTTTGTATCT. Cells were harvested for the subsequent experiments 48 h after transfection.

Immunoblotting

Total proteins of cells and mouse tissues were prepared and resolved by SDS-PAGE and transferred to nitrocellulose membranes, and analyzed by immunoblotting. The primary antibodies used were as follows: anti-L-ferritin (1:1000, cat# ab109373), anti-H-ferritin (1:1000, cat# ab65080), and anti-IRP1 (1:1000, cat# ab183721) from Abcam

(Cambridge, MA); anti-TfR1 (1:5000, cat# 136800) from Thermo Fisher (Waltham, MA); anti-IRP2 (1:1000, polyclonal, selfmade, raised from rabbits)[52]; anti-Aconitase2 (Aco2) (1:1000, cat# 11134-1-AP) from Proteintech Group Inc (Chicago, IN, USA); anti-drosophila ZIP13 (dZIP13, 1:1000) from previous lab stocks[17]; anti-FPN1 (1:1000, cat# NBP1-21502) from Novus Biologicals (Littleton, CO); anti-MYC (1:5000, cat# 2276S) from Cell Signaling Technology (Shanghai, China); anti-HA (1:5000 for Western blot, 1:500 for IP, previously covance cat# MMS-101P) from BioLegend (Ontario, CA); Anti-GST (1:5000, cat# HT601-01), anti-ACTIN (1:10,000, cat# HC201-01), and anti-GAPDH (1:10,000, cat# HC301-01) from TransGen Biotech (Beijing, China). For full scan blots please see the Source Data file. Relative quantification analysis of western blot band intensity was performed using ImageJ (v1.46).

Immunofluorescence

Cells were cultured on glass coverslips in 35-mm glass base dishes and then co-transfected with plasmids pCDNA3.1-hZIP13-MYC and p58-GFP for 24 h. Cells were fixed with 4% paraformaldehyde in PBS, permeabilized with 0.1% Triton X-100 in PBS for 5 min, and then incubated with an anti-MYC antibody. Fluorescence was detected after secondary staining with the Alexa Fluor 594-conjugated $F(ab')_2$ fragment of goat anti-mouse IgG (Thermo Fisher Scientific, cat# A-11020). The localization was determined using confocal microscopy (Nikon A1R HD Confocal Microscope).

Labile iron pool (LIP) measurement

Cytosolic labile iron was measured using the iron-sensitive probes Calcein-AM (Aladdin, Shanghai, China, cat# C273362)[52]. Briefly, 10^6 cells were incubated with 100 nM Calcein-AM in 1 × PBS at 37 °C for 15 min, then washed three times with PBS to remove extracellular Calcein-AM. After centrifugation at 3000 × g for 5 min, the supernatant was removed. The cells were resuspended in 200 µl PBS and transferred to a black 96-well plate. The basal fluorescence was monitored at excitation of 488 nm and emission of 517 nm using the BioTek Synergy H1 Microplate Reader (Shanghai, China). The iron chelator deferiprone (DFP, final concentration 100 µM) was added to dequench the Calcein-iron complex. The fluorescence was monitored within 10 min. The fluorescence difference after and before adding DFP represented as the level of cytosolic LIP. Mitochondrial iron was measured using Rhodamine B-[(1,10-phenanthroline-5-yl)-aminocarbonyl] benzyl ester (RPA, Squarix GmbH, Elbestr, Germany, cat# ME043.1 (RPA.1))[52]. Briefly, 10^6 cells were incubated with 2 µM RPA in Hanks' balanced salt solution (HBSS) for 15 min at 37°C, then washed once and resuspended in 200 µl HBSS for additional 15 min. Then the cells were washed three times and resuspended in 200 µl HBSS. The basal fluorescence was monitored at 543 nm (excitation) and 601 nm (emission) using a fluorescent microplate reader. The mitochondrial chelatable iron was removed from RPA by the addition of excess membrane-permeable iron chelator pyridoxal isonicotinoyl hydrazone (PIH, final concentration 2 mM, MedChemExpress, cat# HY-114758). The difference of the fluorescence between after and before adding PIH represented the mitochondrial LIP. Golgi iron level was measured using FeRhoNox™-1 (Goryo Chemicals, cat# GC901), which selectively stains Fe^{2+} in endolysosomes and Golgi[53]. For the Golgi iron, 10^6 cells were incubated with 5 µM FeRhoNox™-1 in HBSS for 30 min at 37°C, then washed three times and resuspended in 200 µl HBSS. The fluorescence was monitored at an excitation of 543 nm and an emission of 570 nm. Relative quantification analysis of fluorescence intensity was performed using ImageJ (v1.46).

Ferrozine iron assay

Iron content was measured using the colorimetric ferrozine-based assay[54]. About 100 µg total proteins of mouse tissues (total volume 100 µl) were used for iron content detection. 22 µl concentrated HCl (11.6 mol/L) was added to the tissue lysate. The mixed sample was heated at 95°C for 20 min, then centrifuged at 20,000 × g for 30 min. The 90 µl supernatant was transferred very gently into new tube. 36 µl ascorbate (75 mM) was added to reduce the Fe (III) into Fe (II). After 4 min of incubation at room temperature, 36 µl ferrozine (10 mM) and 72 µl saturate ammonium acetate were sequentially added to each tube and the absorbance was measured at 570 nm within 30 min.

Zinpyr-1 staining

MEFs were treated with 50 µM $ZnSO_4$ or with ZIP13 transfection for 24 h before Zinpyr-1 staining. The cells were incubated with 5 µM Zinpyr-1 in DMEM complete medium for 30 min at 37°C, and then washed twice with HBSS. The fluorescent intensity was determined using confocal microscopy (Nikon A1R HD Confocal Microscope).

Iron binding assay

The GST protein and the fusion protein of the N-terminal peptide of mouse ZIP13 with GST tag were obtained by *E.coli* expression and purification. The iron column was generated from Ni-NAT Sefinose™ Resin purchased from Sangon Biotech (Cat#C600033, Shanghai, China). Following the instruction, the Ni was eluted from the Ni column by 10 volumes of stripping buffer (50 mM NaH_2PO_4, 300 mM NaCl, and 100 mM EDTA, pH 8.0). And then the column was washed with 10–20 volumes of deionized water. 5 volumes of $FeCl_2$ buffer (100 mM $FeCl_2$ and 1 M ascorbic acid dissolved in deionized water) or $ZnSO_4$ buffer (100 mM $ZnSO_4$ dissolved in deionized water) was used to load the column, followed by 10 volumes of 1×PBS wash. The GST protein and the fusion protein of the N-terminal peptide of mouse ZIP13 with GST tag were obtained by *E.coli* expression and purification. Equal amounts of purified proteins were passed through the Fe^{2+} or Zn^{2+} column, and then washed with the wash buffer (50 mM NaH_2PO_4, 300 mM NaCl, 10 mM imidazole, pH 8.0) to remove impurities. Finally, the elution buffer (50 mM NaH_2PO_4, 300 mM NaCl, 250 mM imidazole, pH 8.0) was used to elute the Fe^{2+} or Zn^{2+} column. Six tubes of eluent were then collected in succession (E1-E6) to detect whether the protein could bind to Fe^{2+} or Zn^{2+} by commassie brilliant blue staining and western blotting.

Iron- and zinc-transport activities of ZIP13-reconstituted liposome

ZIP13-HA knockin mice were crossed with Alb-cre mice to obtain the liver-specific ZIP13-overexpressed mice (*ZIP13-OE*). The livers of 3 months old WT and *ZIP13-OE* male mice were cut into pieces and then homogenized in 10 ml BufferA (0.32 M) sucrose, 5 mM Tris-HCl (pH 7.5), 120 mM KCl, 1 mM EDTA, 0.2 mM PMSF, 1 µg/ml pepstatin, 1 µg/ml leupeptin, and 1 µg/ml aprotinin. After centrifugation at 800 rpm at 4 °C for 30 min, the supernatants were transferred into the ultracentrifuge tube. After 100,000×g centrifugation for 1 h, the supernatant was discared and the precipitation was lyzed with RIPA (Beyotime, cat# P0013B) for 2 h on the ice. After 12,000×g centrifugation, the supernatant was the total liver membrane protein component. The hZIP13-HA fusion protein was obtained from liver membrane proteins by immunocoprecipitation assay with the help of proteinA/G beads, HA antibody, and HA peptide. The isolated hZIP13-HA was used in the construction of liposomes.

Liposomes were essentially prepared as described previously with some modifications[55]. Liver Total Lipid Extractwas purchased from Avanti Polar lipids (cat# 181104). They were dried under gas nitrogen and then kept under vacuum for at least 3 h, then suspended in 20 mM HEPES, pH 7.4, 100 mM KCl, 10 µM Fe^{2+}, 200 mM sucrose for 60 min at 37 °C, frozen in liquid nitrogen and thawed at 37 °C for five cycles, and extruded through membrane filters of 0.4 µm. The liposomes were destabilized by the addition of 0.5% (w/v) Triton X-100 and incubated for 3 h at room temperature. Purified ZIP13 was added with a protein/lipid ratio of 1:40 (w/w), and incubated for 2 h at 4 °C. Detergents were removed by incubating the mixture with additional Bio-Beads SM2

(Bio-Rad) at a bead (wet weight)/detergent ratio of 100:1 (w/w) overnight at 4 °C with agitation, and repeated once with Bio-Beads SM-2 for 3 ~ 4 h at 4 °C. Proteoliposomes were separated from the Bio-Beads SM-2, and added with the buffer without sucrose to centrifuge at 17,000×g for 20 min at 4 °C. The obtained liposomes needed to be weighted. Subsequently, the pellets of liposome were resuspended in the buffer to a concentration of 20 mg/ml. The same amount of protein-free control and hZIP13-liposome were centrifuged at 17,000×g at 4 °C for 20 min. 10 μM Zn^{2+} was added to the buffer containing 20 mM HEPES (pH 7.4), 100 mM KCl to resuspend the liposomes. The liposomes were placed in an incubator 0 h, 2 h, and 6 h at 37 °C, respectively. The liposomes were washed three times with PBS by centrifuging at 17,000 × g at 4 °C for 20 min. For iron transport detection, liposomes were incubated with 100 nM iron probe calcein, which apparently could permeate liposomes, in 100 μl PBS for 15 min at 37 °C. After centrifuging at 17,000 × g at 4 °C for 20 min, the liposomes were washed 3 times with PBS and suspended by 100 μl PBS. The fluorescent intensity was determined at λex 488 nm and λem 517 nm. For zinc transport detection, liposomes were treated essentially the same as above, and zinc was detected with 10 μM TSQ, a membrane-permeable zinc probe. The fluorescent intensity was determined at λex 334 nm and λem 495 nm.

Proline hydroxylase activity

The ER/Golgi were isolated from WT and *Zip13-KO* cells to analyze the activity of proline hydroxylase. The isolated ER/Golgi was broken by an ultrasonic crusher (power: 600 W; broken: 3 s; pause: 7 s; and 40 cycles). The protein concentrations of ER /Golgi lysates of WT and *Zip13-KO* were determined by BCA (Beyotime, Shanghai, China, cat# P0012S). 100 μg total protein of each preparation was used to detect enzyme activity. The 100 μg total protein was configured by buffer to 50 μl total volume, and then assayed in 480 μl metal-supplemented or non-supplemented buffer containing L-proline substrate (3% morpholine ethanesulfonic acid, 0.3% α-ketoglutaric acid, 0.1% ascorbic acid, 0.2% L-proline, and ddH_2O). 2 μM of iron or zinc ion was added to examine the possible rescuing effect. The reaction mixture was placed in a 35 °C water bath shaker at 200 rpm for 8 min and then heated at 100 °C for 2 min. After centrifugation at 6000 rpm, 200 μl supernatant was collected for the detection of hydroxyproline content. Hydroxyproline contents were measured by a specialized kit (Solarbio, Beijing, China, cat#BC0250). A standard curve was made according to the hydroxyproline standard provided in the kit (standard curve: $y = 0.0897x + 0.0988$). The activity of proline hydroxylase in the sample was calculated according to the formula: enzyme activity (U/g) = [OD(Sample-blank)-0.0988] × V × 1000/(m × t × M × 0.0897). V: total volume of reaction liquid; m: sample quality; t: reaction time; M: molar mass of hydroxyproline, 231. Relative acitvites were normalized by the corresponding protein concentrations.

Quantitative real-time PCR (RT-qPCR)

Total RNA was isolated with TRIzol (Invitrogen, cat# 15596018CN), and cDNA was prepared using the EasyScript® One-Step gDNA Removal and cDNA Synthesis SuperMix (TransGen Biotech, cat# AE311-02). RT-qPCR were performed using *PerfectStart*® Green qPCR SuperMix (TransGen Biotech, cat# AQ601-04-V2) by qTOWER 3 or Bio-Rad CFX Manager (Version 3.1). The primer sequences were provided in Supplementary Table 3 in Supplementary Tables.

Collagen extraction

Collagen was extracted from the cell culture media and mouse skin as previously described[29,56,57]. Briefly, cultures were supplemented with 10% fetal-calf serum and 50 mg/ml ascorbic acid. The medium was collected and then acidified to 3% acetic acid. Subsequently, the medium was digested with 50 mg/ml pepsin at 4°C for 24 h. Collagens were precipitated with 1.0 M NaCl. The skin samples of the mice were minced to pieces and washed extensively twice with a solution containing 3.4 M NaCl, 0.05 M Tris-HCl (pH 7.4), a mixture of protease inhibitors (Roche, Guangzhou, China, cat# 4693132001) and 0.01 mM PMSF to remove serum and noncollagenous proteins. After vigorous mixing for 24 h, the sample was centrifuged at 14,000 × g for 30 min. The pellet was extracted sequentially with 1.0 M NaCl and 0.05 M Tris-HCl (pH 7.4) for 5 days. Extracts were collected by centrifugation at 14,000 × g for 30 min. All procedures were performed at 4°C. The α1 and α2 chains of type I collagen were separated and cut from the SDS-PAGE gel, and then the hydroxylation level was measured by LC-MS.

Ferritin iron staining

To detect ferric iron loading in mouse liver and spleen, protein was extracted from these tissues. The same amount of total protein (1 mg) was heated at 70°C for 10 min, then centrifuged at 12,000×g for 10 min. The supernatant was loaded on each lane and separated on an 8% native-PAGE gel. The gel was stained with Prussian blue staining solution (10% $K_4[Fe(CN)_6]$ and 10% HCl) at room temperature. Iron-loaded ferritin was visible as blue bands.

Hematoxylin and eosin (HE) staining and Masson staining

Mouse tissues were formalin-fixed and paraffin-embedded. Paraffin sections (5 μm) were cut and stained with H&E and Masson staining for histological analysis. Histology images were acquired with Nikon eclipse e200 (Capture2.2.1).

Detection of tissue iron by Perls' staining

Mouse tissue sections were incubated with a mixture of 2% $K_4[Fe(CN)_6]$ and 2% HCl, at room temperature for 1 h. After being washed three times by PBS, the sections were stained with an appropriate amount of diaminobenzidine (DAB, Merck, cat# D5905) dye solution (30 mg DAB + 40 mL Tris (pH7.5) + 1 ml 3% H_2O_2) for 5 min, with observation under an optical microscope (Nikon eclipse e200).

Statistics and reproducibility

GraphPad Prism 5 and Microsoft Excel 2013 were used for statistical analysis. ImageJ were used for image analysis. All analyses were performed with the experimenter blinded to the manipulation that subject mice had received. All experiments were performed at least three times. Both technical and biological replicates were reliably reproduced. The values were expressed as mean ± SD from at least three independent experiments. Student's *t*-test was carried out using SPSS ver. 22.0 software (IBM Corporation, Armonk, NY, USA). Significance was considered at $p < 0.05$.

Reporting summary

Further information on research design is available in the Nature Portfolio Reporting Summary linked to this article.

Data availability

Data generated in this study are included in the manuscript and its Supplementary Information. Source data are provided with this paper.

References

1. Rouault, T. A. Iron metabolism in the CNS: implications for neurodegenerative diseases. *Nat. Rev. Neurosci.* **14**, 551–564 (2013).
2. Rao, R. & Georgieff, M. K. Iron in fetal and neonatal nutrition. *Semin. Fetal Neonatal Med.* **12**, 54–63 (2007).
3. Muckenthaler, M. U., Rivella, S., Hentze, M. W. & Galy, B. A red carpet for iron metabolism. *Cell* **168**, 344–361 (2017).
4. Das, A., Nag, S., Mason, A. B. & Barroso, M. M. Endosome-mitochondria interactions are modulated by iron release from transferrin. *J. Cell Biol.* **214**, 831–845 (2016).

5. Donovan, A. et al. Positional cloning of zebrafish ferroportin1 identifies a conserved vertebrate iron exporter. *Nature* **403**, 776–781 (2000).
6. Donovan, A. et al. The iron exporter ferroportin/Slc40a1 is essential for iron homeostasis. *Cell Metab*. **1**, 191–200 (2005).
7. Drakesmith, H., Nemeth, E. & Ganz, T. Ironing out Ferroportin. *Cell Metab*. **22**, 777–787 (2015).
8. Ganz, T. Cellular iron: Ferroportin is the only way out. *Cell Metab*. **1**, 155–157 (2005).
9. Fujishiro, H., Yano, Y., Takada, Y., Tanihara, M. & Himeno, S. Roles of ZIP8, ZIP14, and DMT1 in transport of cadmium and manganese in mouse kidney proximal tubule cells. *Metallomics* **4**, 700–708 (2012).
10. Steimle, B. L., Smith, F. M. & Kosman, D. J. The solute carriers ZIP8 and ZIP14 regulate manganese accumulation in brain microvascular endothelial cells and control brain manganese levels. *J. Biol. Chem*. **294**, 19197–19208 (2019).
11. van Raaij, S. E. G., Srai, S. K. S., Swinkels, D. W. & van Swelm, R. P. L. Iron uptake by ZIP8 and ZIP14 in human proximal tubular epithelial cells. *Biometals* **32**, 211–226 (2019).
12. Wang, C. Y. et al. ZIP8 is an iron and zinc transporter whose cell-surface expression is up-regulated by cellular iron loading. *J. Biol. Chem*. **287**, 34032–34043 (2012).
13. Liuzzi, J. P., Aydemir, F., Nam, H., Knutson, M. D. & Cousins, R. J. Zip14 (Slc39a14) mediates non-transferrin-bound iron uptake into cells. *Proc. Natl Acad. Sci. USA* **103**, 13612–13617 (2006).
14. Xiao, G. & Zhou, B. ZIP13: A study of drosophila offers an alternative explanation for the corresponding human disease. *Front Genet* **8**, 234 (2017).
15. Zhao, M. & Zhou, B. A distinctive sequence motif in the fourth transmembrane domain confers ZIP13 iron function in drosophila melanogaster. *Biochim. Biophys. Acta Mol. Cell Res*. **1867**, 118607 (2020).
16. Xu, J. X., Wan, Z. H. & Zhou, B. Drosophila ZIP13 is posttranslationally regulated by iron-mediated stabilization. *BBA Mol. Cell Res*. **1866**, 1487–1497 (2019).
17. Xiao, G. R., Wan, Z. H., Fan, Q. W., Tang, X. N. & Zhou, B. The metal transporter ZIP13 supplies iron into the secretory pathway in Drosophila melanogaster. *Elife* **3**, e03191 (2014).
18. Philpott, C. C. Pumping iron. *Elife* **3**, e03997 (2014).
19. Mandilaras, K., Pathmanathan, T. & Missirlis, F. Iron absorption in Drosophila melanogaster. *Nutrients* **5**, 1622–1647 (2013).
20. Tang, X. N. & Zhou, B. Iron homeostasis in Insects: Insights from Drosophila Studies. *Iubmb Life* **65**, 863–872 (2013).
21. Wu, S., Yin, S. & Zhou, B. Molecular physiology of iron trafficking in Drosophila melanogaster. *Curr. Opin. Insect Sci*. **50**, 100888 (2022).
22. Leidgens, S. et al. Each member of the poly-r(C)-binding protein 1 (PCBP) family exhibits iron chaperone activity toward ferritin. *J. Biol. Chem*. **288**, 17791–17802 (2013).
23. Bin, B. H. et al. Biochemical characterization of human ZIP13. *Protein J. Biol. Chem*. **286**, 40255–40265 (2011).
24. Bin, B. H., Hojyo, S., Ryong Lee, T. & Fukada, T. Spondylocheirodysplastic Ehlers-Danlos syndrome (SCD-EDS) and the mutant zinc transporter ZIP13. *Rare Dis*. **2**, e974982 (2014).
25. Jeong, J. et al. Promotion of vesicular zinc efflux by ZIP13 and its implications for spondylocheiro dysplastic Ehlers-Danlos syndrome. *Proc. Natl Acad. Sci. USA* **109**, E3530–E3538 (2012).
26. Fukada, T. et al. The zinc transporter SLC39A13/ZIP13 is required for connective tissue development; its involvement in BMP/TGF-beta signaling pathways. *PLoS One* **3**, e3642 (2008).
27. Huang, L., Kirschke, C. P., Zhang, Y. & Yu, Y. Y. The ZIP7 gene (Slc39a7) encodes a zinc transporter involved in zinc homeostasis of the Golgi apparatus. *J. Biol. Chem*. **280**, 15456–15463 (2005).
28. Woodruff, G. et al. The zinc transporter SLC39A7 (ZIP7) is essential for regulation of cytosolic zinc levels. *Mol. Pharm*. **94**, 1092–1100 (2018).
29. Giunta, C. et al. Spondylocheiro dysplastic form of the Ehlers-Danlos syndrome -: an autosomal-recessive entity caused by mutations in the zinc transporter gene. *Am. J. Hum. Genet*. **82**, 1290–1305 (2008).
30. Tuderman, L., Myllyla, R. & Kivirikko, K. I. Mechanism of the prolyl hydroxylase reaction. 1. Role of co-substrates. *Eur. J. Biochem* **80**, 341–348 (1977).
31. Vasta, J. D. & Raines, R. T. Human collagen prolyl 4-hydroxylase is activated by ligands for its iron center. *Biochemistry* **55**, 3224–3233 (2016).
32. Krane, S. M., Pinnell, S. R. & Erbe, R. W. Lysyl-protocollagen hydroxylase deficiency in fibroblasts from siblings Gs with hydroxylysine-deficient collagen. *Proc. Natl Acad. Sci. USA* **69**, 2899 (1972).
33. Kan, M. N., Fujiwara, T. & Kamiya, T. Golgi-localized OsFPN1 is involved in Co and Ni transport and their detoxification in rice. *Rice* **15**, 36 (2022).
34. Ma, T. et al. A pair of transporters controls mitochondrial Zn(2+) levels to maintain mitochondrial homeostasis. *Protein Cell* **13**, 180–202 (2022).
35. Marchi, S. et al. Mitochondrial and endoplasmic reticulum calcium homeostasis and cell death. *Cell Calcium* **69**, 62–72 (2018).
36. Ogawa, Y., Kinoshita, M., Shimada, S. & Kawamura, T. Zinc and skin disorders. *Nutrients* **10**, 199 (2018).
37. Di Bisceglie, A. M., Axiotis, C. A., Hoofnagle, J. H. & Bacon, B. R. Measurements of iron status in patients with chronic hepatitis. *Gastroenterology* **102**, 2108–2113 (1992).
38. Lin, T. J., Liao, L. Y., Lin, S. Y., Lin, C. L. & Chang, T. A. Influence of iron on the severity of hepatic fibrosis in patients with chronic hepatitis C. *World J. Gastroenterol*. **12**, 4897–4901 (2006).
39. Wang, W., Knovich, M. A., Coffman, L. G., Torti, F. M. & Torti, S. V. Serum ferritin: past, present and future. *Biochim. Biophys. Acta* **1800**, 760–769 (2010).
40. Mao, J. Z. et al. The iron exporter ferroportin 1 is essential for development of the mouse embryo, forebrain patterning and neural tube closure. *Development* **137**, 3079–3088 (2010).
41. Jiang, B. et al. Hephaestin and ceruloplasmin facilitate iron metabolism in the mouse kidney. *Sci. Rep*. **6**, 39470 (2016).
42. Weiss, A. et al. Orchestrated regulation of iron trafficking proteins in the kidney during iron overload facilitates systemic iron retention. *PLoS One* **13**, e0204471 (2018).
43. van Raaij, S. et al. Tubular iron deposition and iron handling proteins in human healthy kidney and chronic kidney disease. *Sci. Rep*. **8**, 9353 (2018).
44. Gunshin, H. et al. Slc11a2 is required for intestinal iron absorption and erythropoiesis but dispensable in placenta and liver. *J. Clin. Invest* **115**, 1258–1266 (2005).
45. Illing, A. C., Shawki, A., Cunningham, C. L. & Mackenzie, B. Substrate profile and metal-ion selectivity of human divalent metal-ion transporter-1. *J. Biol. Chem*. **287**, 30485–30496 (2012).
46. Jenkitkasemwong, S. et al. SLC39A14 deficiency alters manganese homeostasis and excretion resulting in brain manganese accumulation and motor deficits in mice (vol 115, pg E1769, 2018). *Proc. Natl Acad. Sci. USA* **115**, E4730–E4730 (2018).
47. Xin, Y. J. et al. Manganese transporter Slc39a14 deficiency revealed its key role in maintaining manganese homeostasis in mice. *Cell Discov*. **3**, 17025 (2017).
48. Jenkitkasemwong, S. et al. SLC39A14 is required for the development of hepatocellular iron overload in murine models of hereditary hemochromatosis. *Cell Metab*. **22**, 138–150 (2015).

49. Zhang, T. et al. Crystal structures of a ZIP zinc transporter reveal a binuclear metal center in the transport pathway. *Sci. Adv.* **3**, e1700344 (2017).
50. Roberts, C. S., Ni, F. & Mitra, B. The zinc and iron binuclear transport center of ZupT, a ZIP transporter from Escherichia coli. *Biochemistry* **60**, 3738–3752 (2021).
51. Rossi, A. et al. Genetic compensation induced by deleterious mutations but not gene knockdowns. *Nature* **524**, 230–233 (2015).
52. Li, H. H. et al. Iron regulatory protein 2 modulates the switch from aerobic glycolysis to oxidative phosphorylation in mouse embryonic fibroblasts. *Proc. Natl Acad. Sci. USA* **116**, 9871–9876 (2019).
53. Hirayama, T., Okuda, K. & Nagasawa, H. A highly selective turn-on fluorescent probe for iron(II) to visualize labile iron in living cells. *Chem. Sci.* **4**, 1250–1256 (2013).
54. Li, H. H. et al. Iron regulatory protein deficiency compromises mitochondrial function in murine embryonic fibroblasts. *Sci. Rep.* **8**, 5118 (2018).
55. Zhang, Y. et al. Structural insights into membrane remodeling by SNX1. *Proc. Natl Acad. Sci. USA* **118**, e2022614118 (2021).
56. Igoucheva, O. et al. Fibulin-4 E57K knock-in mice recapitulate cutaneous, vascular and skeletal defects of recessive cutis laxa 1B with both elastic fiber and collagen fibril abnormalities. *J. Biol. Chem.* **290**, 21443–21459 (2015).
57. Steinmann, B. et al. Evidence for a structural mutation of procollagen type I in a patient with the Ehlers-Danlos syndrome type VII. *J. Biol. Chem.* **255**, 8887–8893 (1980).

Acknowledgements

This study was supported by the National Key Research and Development Program of China (2023YFA0915403 to B.Z.), the National Natural Science Foundation of China (32371226 to B.Z. and 32000821 to H.L.), Shenzhen Science and Technology Program (KQTD20180413181837372 to B.Z.), Shenzhen Institute of Advanced Technology startup fund, and the Natural Science Foundation of Guangdong Province (2022A1515012236 to H.L.).

Author contributions

H.L. and B.Z. conceived and designed experiments. H.L., Y.C., Y.H., M.Z., and X.P. performed experiments. K.L. and F.S. contributed to data analysis. H.L. and B.Z. wrote the manuscript.

Competing interests

The authors declare no competing interests.

Additional information

Supplementary information The online version contains supplementary material available at https://doi.org/10.1038/s41467-024-55149-2.

Correspondence and requests for materials should be addressed to Bing Zhou.

Peer review information *Nature Communications* thanks Chonglin Yang and the other, anonymous, reviewer(s) for their contribution to the peer review of this work. A peer review file is available.

Reprints and permissions information is available at http://www.nature.com/reprints